Materials Today Physics 42 (2024) 101388

Contents lists available at ScienceDirect

Materials Today Physics

journal homepage: www.journals.elsevier.com/materials-today-physics

Structural dynamics of first-order phase transition in giant magnetocaloric $La(Fe,Si)_{13}$: The free energy landscape

André Azevedo Beleza [a], Bernardo Pires [a], Rafael Almeida [a], John S.O. Evans [b], António M. dos Santos [c], Mathias Frontzek [c], Edmund Lovell [d], Benedikt Beckmann [e], Konstantin Skokov [e], Oliver Gutfleisch [e], João Pedro Araujo [a], A.M. Milinda Abeykoon [f], João S Amaral [g], João Horta Belo [a,*]

[a] IFIMUP, Laboratory for Materials and Emergent Technologies (LAPMET), Departamento de Física e Astronomia, Faculdade de Ciências, Universidade do Porto, Rua do Campo Alegre s/n, 4169-007, Porto, Portugal
[b] Department of Chemistry, Durham University, Durham, DH1 3LE, United Kingdom
[c] Neutron Scattering Division, Oak Ridge National Laboratory, Oak Ridge, TN, 37831-6475, USA
[d] Camfridge Ltd., Milton Keynes, MK2 3HU, United Kingdom
[e] Institute of Materials Science, Technical University of Darmstadt, 64287, Darmstadt, Germany
[f] National Synchrotron Light Source II, Brookhaven National Laboratory Upton, NY, 11973, USA
[g] Department of Physics and CICECO, University of Aveiro, Campus of Santiago, 3810-193, Aveiro, Portugal

A B S T R A C T

Maximizing the performance of magnetic refrigerators and thermomagnetic energy harvesters is imperative for their successful implementation and can be done by maximizing their operation frequency. One of the features delimiting the frequency and efficiency of such devices is the phase transition kinetics of their magnetocaloric/thermomagnetic active material. While previous studies have described the magnetic component governing the kinetics of the magnetovolume phase transition in $La(Fe,Si)_{13}$ giant magnetocaloric materials, a comprehensive description of its structural component has yet to be explored. In this study, in situ synchrotron X-ray diffraction is employed to describe the structural changes upon magnetic field application/removal. Long magnetic field dependent relaxation times up to a few hundred seconds are observed after the driving field is paused. The phase transition is found to be highly asymmetric upon magnetic field cycling due to the different Gibbs energy landscapes and the absence of an energy barrier upon field removal. An exponential relationship is found between the energy barriers and the relaxation times, suggesting the process is governed by a non-thermal activation over an energy barrier process. Such fundamental knowledge on first-order phase transition kinetics suggests pathways for materials optimization and smarter design of magnetic field cycling in real-life devices.

1. Introduction

The growing interest in developing environmentally friendly and energetically efficient heating and cooling devices is a direct consequence of ongoing efforts towards climate change mitigation and economic growth [1–4]. Magnetic heat pumping devices that employ magnetocaloric materials have long stood out as offering a promising contribution to the aforementioned challenges. These devices are capable of operating with a higher energy efficiency [5], thus potentially cutting down on CO_2-emissions associated with their power consumption, as well as eliminating the need for high global warming or ozone-depleting gases required by currently employed vapor-compression devices [6].

In general, through adiabatic changes of an external driving field, the temperature of caloric materials can be altered [7]. When this driving field is an external magnetic field, the effect is known as the magnetocaloric effect, and the adiabatic temperature change (ΔT_{ad}) and the isothermal entropy change (ΔS_{iso}) play a key role in establishing the applicability and competitiveness of each material for heating and cooling applications [8–10]. As the ΔT_{ad} and ΔS_{iso} observed in the vicinity of these materials' phase transitions is typically higher in those undergoing a first-order phase transition (FOPT) [11], when compared to a second-order phase transition (SOPT), there have been considerable efforts in optimizing the overall performance of FOPT materials [12–18].

$La(Fe,Si)_{13}$-based materials exhibit the giant magnetocaloric effect (GME) with most prominence near their Curie temperature (T_C), associated with their ferromagnetic (FM) to paramagnetic (PM) FOPT [19,20], making them very promising candidates for magnetic refrigeration [21,22] and thermomagnetic energy harvesting [1,23,24]. In addition to

* Corresponding author.
E-mail address: jbelo@fc.up.pt (J.H. Belo).

https://doi.org/10.1016/j.mtphys.2024.101388
Received 13 January 2024; Received in revised form 1 March 2024; Accepted 2 March 2024
Available online 5 March 2024

being constituted by relatively abundant materials, La being amongst the most abundant rare earth element, their T_C has been reported to be highly tunable by chemical substitution, such as by partial substitution of Fe with Mn or Co, resulting in a decrease or increase in T_C [25,26], respectively. The transition temperature remains unchanged upon particle size reduction with a decrease in hysteresis loss, albeit at the expense of a less sharp transition [14,20,27]. Additionally, hydrogenation of the material brings its T_C closer to room temperature, enabling applications of the material at ambient temperature while maintaining excellent magnetocaloric properties [13,28].

Such $LaFe_{13-x}Si_x$-based compounds with $1.2 < x < 2.6$ compositions crystallize in a cubic $NaZn_{13}$-type structure (space group $Fm\bar{3}c$), with the La, 8a and Fe1, 8b sites fixed at the fractional coordinates (1/4,1/4,1/4) and (0,0,0), and further Fe2 and Si atoms occupying the 96i sites at the set of positions (0,y,z) [19,29]. Parallel to the formation of these alloys, α-Fe is a commonly found secondary phase induced by the presence of a La-rich phase, which typically represents 5–8% wt [29–31].

As $LaFe_{13-x}Si_x$ with $x < 1.6$ is heated above T_C, a first-order FM to PM transition occurs, and these alloys undergo a large discontinuous isostructural volumetric change of about 1% that is characterized by a negative thermal expansion coefficient [20,30,32]. The lattice parameter is strongly dependent on the magnetic moment of Fe atoms, giving rise to the strong magnetovolume coupling nature of this FOPT [19,33,34]. Furthermore, the increase in T_C by the addition of hydrogen and chemical substitution of Fe with other transition materials has been explained by the lengthening of the Fe1–Fe2 distances which is thought to promote stronger FM exchange interactions [19,29].

In spite of their advantages, FOPT magnetocaloric materials, including $La(Fe,Si)_{13}$, bring forth a set of challenges pertaining to hysteretic losses [35], phase transition asymmetries [36] and phase transition dynamics [20,37], which can hinder their performance in real world energy-efficient cyclable devices. In particular, the study of temperature-dependent measurements has revealed the crucial role internal pressure and strain has in establishing the asymmetry of the phase transition [14,36,38–40]. Meanwhile, the kinetics of the phase transition plays a critical role in determining the rate at which a material may be cycled for optimal performance [41–46], since an incomplete phase transition is inherently associated with a suppressed thermal response. As a result, the optimization of FOPT magnetocaloric devices must reflect the inherent asymmetry of the phase transition, while also facing the trade-off between maximizing their operation frequency and ensuring maximal ΔT_{ad} yield.

Previous studies have set out to characterize the relaxation mechanisms that underpin the magnetic component of the FOPT in several magnetocaloric materials [20,25,47] and have reported that the magnetization relaxation is highly dependent on the sample's shape, temperature and magnetic field, resulting in extended relaxation times, reaching tens to hundreds of seconds when subjected to magnetic fields close to the onset of the FOPT [20].

These relaxation processes have historically been modeled through thermal activation models [47,48], variations of the Bean-Rodbell model [49,50] and by Landau-based models [42]. Meanwhile, density functional theory has been successful at predicting the correlation between the large magnetovolume effects and the itinerant metamagnetic phase transition of the $La(Fe,Si)_{13}$ family [51]. In particular the Fe-partial electronic density of states, together with its sublattice and itinerant electron magnetism, induces pronounced lattice softening and significant lattice contributions to the total entropy change [52–54]. This provides further insight on these materials' strong magnetovolume coupling.

Despite the above, there is still a lack of experimental observations and fundamental understanding of the dynamics of the magnetic field driven structural phase transition, as opposed to being temperature-driven, and, since these are coupled, its interplay with the magnetic transition. As such, in this work we investigate the kinetics and the asymmetry of the isostructural phase transition through time-resolved X-ray diffraction at the National Synchrotron Light Source II (NSLS II) at Brookhaven National Laboratory [55], with the aim of shedding light on the relationship between the magnetic and structural phase transitions, and to assess how the two are time (de)coupled using the compound $LaFe_{11.6}Si_{1.4}$ as a case study material. Lastly, the observed time dependence and asymmetries of the phase transition are evaluated and explained through direct comparison with the magnetization and volume dependent free energy landscape of a compressible 3D Ising lattice.

2. Results and discussion

2.1. Time dependence of the crystal structure changes

To carry out a detailed structural analysis of the magnetic field induced phase transition in a $LaFe_{11.6}Si_{1.4}$ sample, a large data set of high brilliance X-ray diffraction patterns was acquired as a function of time, temperature, and external magnetic field (with varying intensity, field sweeping direction and sweeping rate).

Inspired by the work of E.Lovell and co-authors on the magnetic phase transition dynamics of $LaFe_{11.6}Si_{1.4}$ [20], a measurement protocol was followed to determine the relaxation of the atomic structure upon magnetic field application on a powder sample with a typical size of 4.5 μm and size distribution as detailed in Fig. S10 in the Supplemental Material [56]. First, the sample was cooled to the measurement temperature, a few Kelvin above T_C, and allowed to reach thermal equilibrium for 15 min. At this point, the X-ray diffraction pattern acquisition was started with a 2 s time resolution. Then, to magnetically induce the phase transition, a magnetic field was applied at a fixed sweep rate up to a given value, H_{pause}, and kept constant thereafter. This allowed the detection of non-field driven relaxation effects, as illustrated in Fig. 1a). Subsequently, the phase evolution was measured as the magnetic field was decreased, from H_{pause} to zero, enabling the structural dynamics to be followed during complete magnetic field cycles. In between these cycles, a thermal reset to the paramagnetic phase was performed by heating the sample up to $T = T_C + 40$ K.

Exploratory neutron diffraction studies successfully allowed the time dependent tracking of the structural component of the phase transition, as shown in Fig. S1 in the Supplemental Material [56]. However, due to the comparatively weak magnetic signature, and the relatively low neutron flux, these measurements ultimately lacked the necessary time resolution to adequately probe the observed relaxation phenomena. Nevertheless, these allowed the magnetic and structural components of the phase transition to be tracked simultaneously with a resolution down to 10 s.

Nevertheless, the high X-ray brilliance at NSLS II allowed for a comprehensive examination of the time evolution of the sample's atomic structure, as clearly demonstrated by the (4 2 2) diffracted peak shown in Fig. 1b), where the presented diffraction patterns were collected at the illustrative temperature of $T = T_C + 10.5$ K, and at different times after the magnetic field had been paused at $\mu_0 H = 2.3$ T. Here, the mean diffraction peak position is seen to shift to lower 2θ values after the magnetic field had been paused, which is consistent with partially overlapping peaks from the sample's first-order field-driven isostructural phase transition, from a low-volume PM state towards a high-volume FM state [28,57]. A more extensive 3D view of the data is given in Fig. S2c) in the Supplemental Material [56].

When peaks at higher scattering angles were analyzed, as shown in Fig. S2a) in the Supplemental Material [56], the application of a magnetic field was revealed to split each of the zero-field peaks, signaling the coexistence of the PM (low-volume) and the FM (high-volume) phases, consistent with a first order transition.

As such, a two-phase model for the Rietveld fitting of the X-ray diffraction data was employed. In Fig. 1c) an example of such a Rietveld refinement is shown, showing good agreement between the measured and the calculated patterns. With this model, the simultaneous tracking

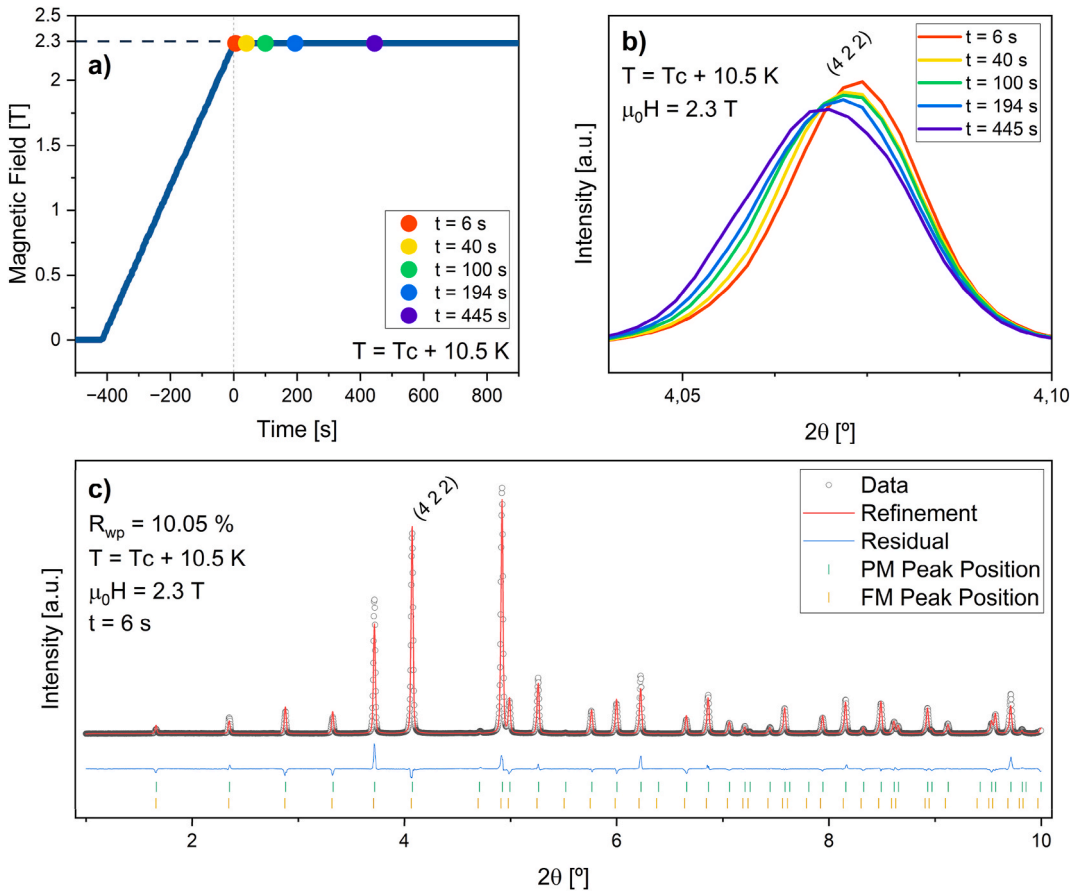

Fig. 1. a) Profile of the applied magnetic field as a function of time describing its application at a constant sweep rate of 5.4 mT s^{-1} up to $\mu_0 H_{pause} = 2.3$ T, at which point the time is set to zero. b) Time evolution of the X-ray diffraction pattern's (4 2 2) peak for the representative set of points identified as colored dots in a) after the applied field is paused at $\mu_0 H_{pause} = 2.3$ T at 10.5 K above the zero-field PM to FM transition (T_C). c) Illustrative diffraction pattern of the sample at $t = 6$ s (black open circles), together with the Rietveld fit (red line) and the difference between the two (blue line). The Bragg reflection angles (vertical green bars) for the PM phase are also shown. (For interpretation of the references to color in this figure legend, the reader is referred to the Web version of this article.)

of the individual cell parameter (a) of each phase and their phase fraction (f) as a function of time was possible, as observed in Fig. S3 in the Supplemental Material [56]. By combining each of these fractions with its corresponding cell parameter, the time evolution of the weighted cell parameter was calculated as follows in Equation (1).

$$\langle a \rangle = a_{PM} f_{PM} + a_{FM} f_{FM} \quad (1)$$

As shown in Fig. 2a) and Fig. 2b) for a given temperature and set of values of H_{pause}, the FM phase fraction (f_{FM}) and the weighted cell parameter ($\langle a \rangle$) exhibit relaxation beyond the point in time at which the magnetic field is paused (set as $t = 0$, for easy reference), allowing for the determination and comparison of the relaxation times observed for each of the different experiments performed.

Inspection of the relaxation profiles presented in Fig. S3 in the Supplemental Material [56], in particular the relaxation measurement with $\mu_0 H_{pause} = 1.6$ T at 7.5 K above T_C, reveals the profile of the weighted lattice parameter to be a result of the increase of the FM phase fraction after the magnetic field is paused, and subsequent decrease of the complementary PM phase fraction, coupled with an increase of the PM lattice parameter and decrease of the FM lattice parameter, as had previously been reported [36]. In turn, this may be quantified as 7% of the FM phase having been induced while driving the external field, and an additional fraction of 46% arising after the magnetic field had been halted (when $t > 0$ s). Simultaneously, during the application of the magnetic field, the lattice parameter of the FM phase decreased by approximately 0.1% and stayed constant thereafter. In contrast, the PM lattice parameter increased by almost 0.05% due to magnetic field application and an additional 0.03% during relaxation. In this analysis, a typical error of around 0.5% is observed in the phase fraction profiles, and a variation of approximately 0.002% in those of the lattice parameters.

To establish the effects of thermal fluctuations and other experimental factors that might influence these conclusions, the time evolution of a zero-field measurement series was inspected and compared to that of a $\mu_0 H_{pause} = 1.1$ T measurement series, as shown in Fig. 2c). Given the time-invariant nature of the zero-field data and the starting value of the presented curves, the observed evolution of the lattice parameter can be safely attributed to the kinetics of the magnetic-field induced phase transition.

2.2. Magnetic field dependence of the structural relaxation

A detailed study of the effects of pausing the magnetic field at different field strengths, H_{pause}, on the observed structural relaxation was conducted at magnetic fields around and above a critical field, H_{c1}. H_{c1} is defined, as shown in Fig. S4 in the Supplemental Material [56], as the minimum field required to onset the PM to FM phase transition of the material at each of the temperatures specified [20].

In Fig. 2b), an increase in the relaxation time of the weighted lattice parameter is observed when $\mu_0 H_{pause} = \mu_0 H_{c1} = 1.6$ T. This increase is followed by a gradual decrease as H_{pause} further increases, as observed in the corresponding relaxation time constants (τ), shown in Fig. 2d). These time constants were calculated from k and η through a fit of the kind $f_{FM}(t) = f_{sat} - f_{rel}\, exp(-kt^{\eta})$, as illustrated in Fig. 2 and discussed in the

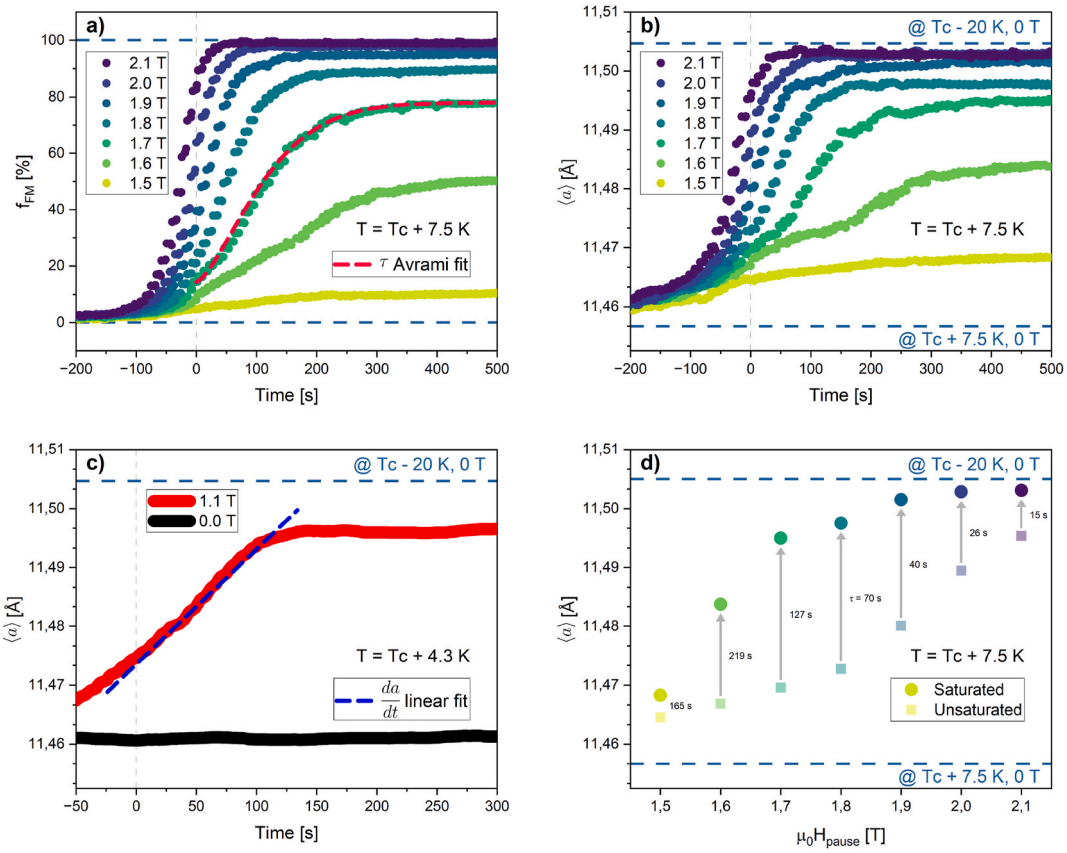

Fig. 2. Relaxation of the a) FM phase fraction and b) weighted lattice parameter as a function of time after the applied magnetic field is driven at 5.4 mT s^{-1} and paused at varying field strengths at 7.5 K above T_C. c) Time evolution of the weighted lattice parameter, 4.3 K above T_C, showcasing the role of the magnetic field on triggering the material's isostructural phase transition (red) in comparison with a zero-field equilibrium measurement series (black). The a) Avrami and c) linear fits (dashed lines) are shown as employed to extract the relaxation rate (da/dt) and relaxation time constant (τ), as presented in Fig. 3 d) The observed unsaturated (t = 0 s) and saturated (t = 500 s) values of the lattice parameter as a function of applied magnetic field for the relaxation profiles presented in b), together with the time constant separating the two states, as presented in Fig. 3 b). The horizontal dashed lines delimit the temperature and phase fraction bounds of the structural transition at the specified conditions. (For interpretation of the references to color in this figure legend, the reader is referred to the Web version of this article.)

next section. Similarly, it is also around this magnetic field that a large increase of the saturated weighted lattice parameter and FM phase fraction is observed, with progressively smaller increases as $\mu_0 H_{pause}$ further increases, as shown in Fig. 2d). The dependence of the lattice parameter with magnetic field strength and time is similar to that reported for the magnetization of the bulk alloy by Lovell and co-authors' previous work following the same H_{pause} protocol [20]. However, the observed structural kinetics occur on a much longer time scale than those reported for the magnetization, which, in the cited work, peaked at around 25 s under similar experimental conditions.

Due to the presence of small plateaus in certain relaxation profiles of the phase fraction, along with disturbances in the time evolution of the lattice parameter of each individual phase, some plateaus occur in the time evolution of the weighted lattice parameter, as shown in Fig. S3 in the Supplemental Material [56] and in Fig. 2a) and b). These resemble the plateaus observed in the relaxation of magnetization, and those observed in the magnetization and phase fraction upon heating/cooling in previous reports [20,36]. This effect is most pronounced at magnetic field values of 1.6 T, 1.7 T, and 1.8 T and occurs around the same phase fraction, where structural relaxation consistently displays a two-step behavior. These plateaus are not observed when those fractions are surpassed by driving to a higher magnetic field. Given the powdered nature of the sample and its caloric properties, these plateaus highlight the significant role played by thermal linkage within the sample in influencing the relaxation profiles.

2.2.1. *Evaluation of the structural relaxation*

To facilitate the comparison of our results with those reported by Lovell and co-authors for the magnetization [20], the lattice parameter's relaxation in time was characterized by its slope, achieved through a linear fit to the beginning of the relaxation of the lattice parameter, as presented in Fig. 2c), which quantifies how fast the lattice parameter expands towards saturation as the magnetic field is paused at a given value. As shown in Fig. 3a), when the pausing magnetic field is increased past the value of the critical field H_{c1}, the relaxation rate increases in a linear fashion. These results are consistent with what is observed in Fig. 2b), where higher H_{pause} values are shown to reach their respective saturation lattice parameter sooner. Additionally, Fig. 3a) demonstrates that temperature does not influence the lattice parameter's relaxation rate, with no differences being observed for the magnetic fields tested, suggestive of a phenomenon that is not thermally activated. When plateaus were observed in a relaxation profile, only the major relaxation process was considered, as it exhibited identical characteristics to the others.

The lattice parameter relaxation rate results are in excellent agreement with what has been reported for the magnetic field dependence of the magnetization relaxation rate by Lovell and co-authors [20], aside from the unobserved plateau of the relaxation rate at high magnetic fields, which is attributed to the set of magnetic fields tested not having been of high enough intensity to saturate the phase transition during field application. However, in the cited work, the magnetization's relaxation rate was reported to decrease and subsequently vanish as the temperature of the alloy was raised up to 13.5 K above T_C, which is in

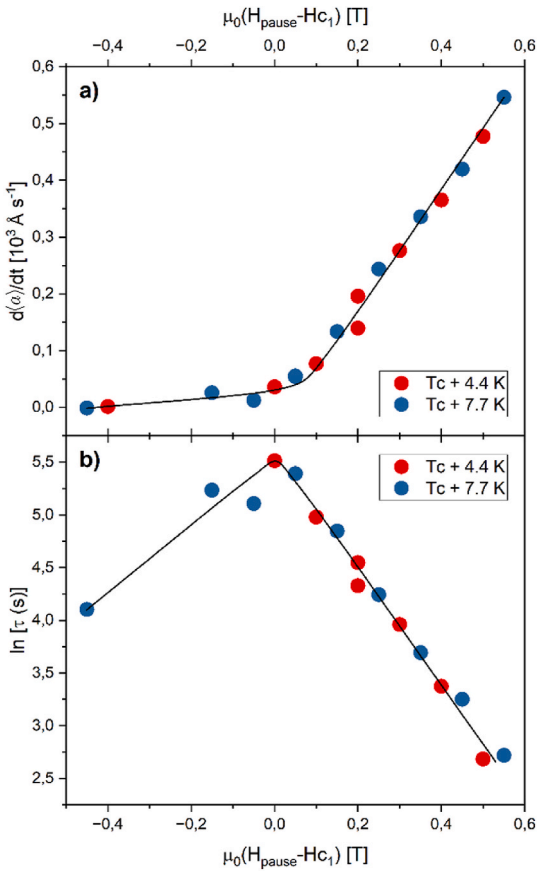

Fig. 3. a) Lattice parameter relaxation rate (da/dt) and b) natural logarithm of the relaxation time constant (τ) of the FM phase fraction as a function of $\mu_0(H_{pause}\text{-}H_{c1})$. The relaxation rate (d$a$/d$t$) was derived from linear fits to the weighted lattice parameter's relaxation, presented in Fig. 2c), as the magnetic field is paused. The relaxation time constant was obtained from fitting the phase fraction's relaxation to the Kolmogorov-Johnson-Mehl-Avrami relation and calculated as $\tau = k^{-1/\eta}$.

contrast with the insignificant temperature related changes observed for the lattice parameter's relaxation rate described here. Comparing the relaxation rates of the lattice parameter and the magnetization, measured from the same sample, as shown in Fig. S5 in the Supplemental Material [56], demonstrated that they exhibit slightly different behavior. Notably, the magnetization exhibits higher relaxation rates compared to the lattice parameter and reaches its saturated value at a magnetic field closer to H_{c1}.

The experimental phase fraction's relaxation profiles were fitted with the adapted Kolmogorov-Johnson-Mehl-Avrami (KJMA) relation, $f_{FM}(t) = f_{sat} - f_{rel}\, exp(-kt^{\eta})$ [58], as shown in Fig. 2a) and Fig. S6 in the Supplemental Material [56]. Here, k is related to the activation energy, η is the Avrami exponent, f_{sat} is the saturated value of the FM phase fraction and f_{rel} is the relaxation's contribution to f_{sat}. This yielded the outcomes presented in Fig. 3b).

Here a peak in relaxation time constant (τ), calculated as $k^{-1/\eta}$, is observed when the pausing magnetic field is equal to that of the critical field H_{c1}. Furthermore, the exponential decrease of τ observed with increasing values of H_{pause}, together with its invariant temperature dependence, is consistent with the above presented increase of the lattice parameter's relaxation rate. While these findings further highlight the importance of phase transition dynamics in overcoming the structural relaxation observed, and hence maximizing cyclability, they also suggest that temperature has a negligible effect on these dynamics (for the temperature range tested), outside of determining the critical field (H_{c1}) at which the phase transition is triggered. Once again, this is an unexpected feature, given the magnetovolume nature of the phase transition and the reported relaxation process for the magnetization of $LaFe_{11.6}Si_{1.4}$, which was found to be neither thermally activated nor athermal [20]. Lastly, the Avrami exponents (η) of the KJMA fits yield values between 0.7 and 1.6 which, when plotted against $\mu_0(H_{pause}\text{-}Hc_1)$, exhibit a general trend towards decreasing η as the magnetic field is increased past the value of Hc_1, as shown in Fig. S11 in the Supplemental Material [56]. This is suggestive of an instantaneous growth with constant nucleation rate [49,50,59].

2.2.2. *Transition direction asymmetry*

The phase evolution was investigated for the span of a full magnetic field cycle (field application and halt followed by field removal), enabling the assessment of the (a)symmetry of the phase transition kinetics. As evidenced by Fig. 4a) and 4b), there is a striking contrast between the time-dependent phase evolution on ramping the field up (forward transition) versus ramping the field down (backwards transition). In the latter, there is no observable time-dependent structural relaxation, as the isostructural transition is completed while the field is still ramping down. This was consistent across all tested temperatures, ranging from $T_C + 4.4$ K up to $T_C + 10.5$ K, during field removal at 5.4 mT s^{-1}.

Interestingly, this time-dependent asymmetry between the forward and backward directions of the structural phase transition was also observed for its magnetization counterpart under identical conditions (temperature, H_{pause} and field sweep rate), as can be seen in Fig. S7 in the Supplemental Material [56]. Additionally, this temporal asymmetry mimics what is observed during temperature cycling, where the phase transition is sharper upon heating into the PM state, as compared to cooling into the FM state [36]. Therefore, the similarity between the transition asymmetry upon magnetic field application/removal and the transition asymmetry upon sample cooling/heating is reinforced [60]. In bulk materials, this has been postulated to arise from neighboring crystals competing for space as they increase in volume [14,36]. However, as will be demonstrated below, the time-dependent asymmetry of the magnetovolume phase transition here presented can be explained on the grounds of the different energy landscapes and their corresponding energy barriers.

The effect of varying the magnetic field sweep rate can be observed in Fig. S8 in the Supplemental Material [56], where a clear increase in the lattice parameter's relaxation time constant (τ) is observed with increasing sweep rate, going from 94 to 107–123 s, at 1.8 mT s^{-1}, 3.6 mT s^{-1} and 5.4 mT s^{-1}, respectively. Despite this, the total time taken for the material to undergo the magnetic field induced transition, including the magnetic field application time, decreases as the magnetic field sweep rate is increased, which is in agreement to what has previously been reported for the magnetic phase transition of the alloy [20].

2.3. *Modelling of the magnetovolume phase transition*

To gain further insight on the experimentally observed structural and magnetic kinetics of $LaFe_{11.6}Si_{1.4}$, a model Hamiltonian was constructed comprising a compressible 3D lattice of Ising spins, where the interaction energy includes magnetovolume coupling [61].

$$\mathscr{H} = -\frac{1}{2}\sum_{i,j}\left[J(v)S_{iz}S_{jz}\right] + \frac{1}{2}Kv^2 - MH \qquad (2)$$

In Equation (2), J is the magnetic exchange parameter between nearest neighbor spins S_{iz} and S_{jz}, v is the volume, and K the compressibility. The dependence of J on volume is given by $J(v) = J_0 + \dot{J}(v - v_0)/v_0$, where v_0 is the volume at the paramagnetic limit, with corresponding J_0. $\dot{J}$ is the parameter that drives the first-order transition and, along with K, was adjusted to best match the experimental data. The simulated lattice is of a cubic array of Ising spins, each representing an (Fe,Si) icosahedron of the $LaFe_{11.6}Si_{1.4}$ unit cell [19,29]. A reasonable

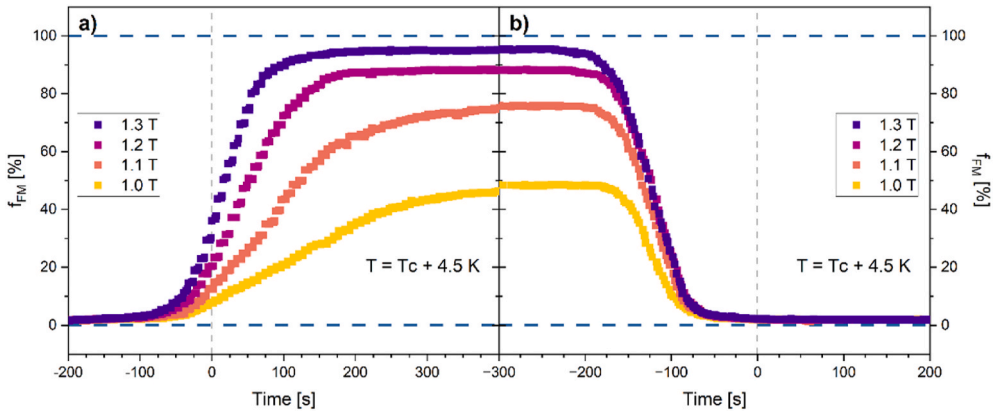

Fig. 4. Relaxation profiles of the FM phase fraction as a function of time as the magnetic field is paused a) after application, up to the presented values of $\mu_0 H_{pause}$, and b) after its removal, from these same values until 0 T, where $t = 0$ s corresponds to the time when the magnetic field reaches 0 T.

agreement between experimental isothermal magnetization data and simulated data, particularly for the critical field dependence on temperature, is reached, as shown in Fig. S9b) in the Supplemental Material [56]. Albeit simpler than other spin vector models, the 3D Ising model with magnetovolume coupling provides a thermodynamically sound physical interpretation of the system under study.

Appropriate parameters in Equation (2) were determined by fitting to experimental data, namely the cell parameter and magnetization data measured as a function of temperature and magnetic field. Typical fits are illustrated in Fig. S9a) in the Supplemental Material [56]. The Gibbs free energy of $LaFe_{11.6}Si_{1.4}$ was then simulated for a wide range of temperatures, magnetic fields, magnetization, and cell parameter

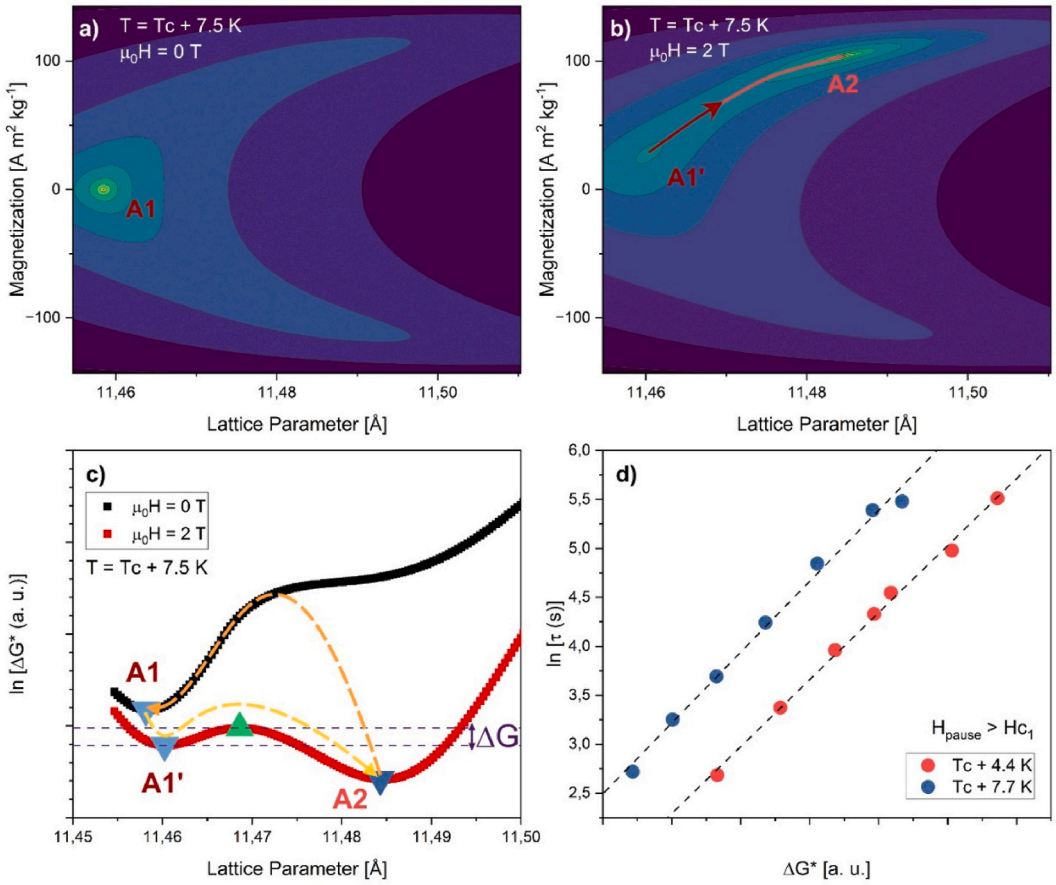

Fig. 5. Contour plots of the simulated Gibbs free energy landscapes of $LaFe_{11.6}Si_{1.4}$ as a function of the lattice parameter and the magnetization 7.5 K above T_C at a) 0 T and b) 2 T. These contour plots, from low (yellow) to high (purple) energy values, show a single minimum at 0 T, denoted as A1, which is replaced by two minima at 2 T, denoted as A1′ and A2, as highlighted in each plot. c) The Gibbs free energy landscape of the lattice parameter is shown for 0 T and 2 T, with an arbitrary scale, together with the route taken by the value of the lattice parameter for magnetic field application (yellow arrow), and for magnetic field removal (orange arrow). The local maximum and minima are represented by up and down triangles, respectively. The energy barrier (ΔG*) is represented by the horizontal purple dashed lines. d) The natural logarithm of the relaxation time constant (τ) as a function of the energy barrier (ΔG*) for magnetic fields above H_{c1}. Linear regressions to both temperatures' curves are presented, demonstrating these are near parallel and hence temperature invariant. (For interpretation of the references to color in this figure legend, the reader is referred to the Web version of this article.)

values. As presented in Fig. 5a) and 5b), these were then grouped to form 2D contour plot maps of the energy landscape of the system for a given temperature and magnetic field.

As observed in Fig. 5a), the energy landscape at zero magnetic field and at T_C + 7.5 K predicts a single minimum of the Gibbs energy, denoted by A1. This minimum is then replaced by two local minima when a magnetic field of 2 T is applied: one minimum in the vicinity of the 0 T minimum, denoted as A1'; and another which occurs at high magnetization and high lattice parameter values, denoted as A2. Inspection of the energy profile as a function of lattice parameter, shown in Fig. 5c), reveals the minimum A2 to have a lower energy value than A1', hence corresponding to the global minimum, and thus a stable state. The A1 and A2 states correspond to the experimentally measured lattice parameter (and magnetization) states observed at 0 T and 2 T, respectively.

As such, during the transition from the local minimum A1' (metastable state) to the absolute minimum A2 (stable state), the system must first traverse an upward energetic slope to reach the saddle point (path section in dark red) and then descend towards A2 (path section in light red in Fig. 5b)). The saddle point which separates these minima is indicative of an energy barrier which must be overcome for the system to reach its lowest energy state from its initial metastable state. For a given temperature and magnetic field combination, the height of this barrier (ΔG^*), represented in Fig. 5c), was calculated and is plotted in Fig. 5d) as a function of the experimentally observed relaxation time constant (τ) previously presented in Fig. 3b). Additionally, for a given field, an increase in temperature above T_C resulted in an increase of the energy barrier.

As shown, an increase in the energy barrier can be linearly correlated with an increase in the natural logarithm of the relaxation time for magnetic fields above H_{c1}. The linearity of the logarithm of the relaxation time constant with the simulated energy barrier is indicative of a nucleation and growth process by activation over an energy barrier. In contrast to the previously reported thermally activated growth process observed in the magnetically induced FOPT of $Gd_5(Si_{0.5}Ge_{0.5})_4$ [47], the parallel slopes found in Fig. 5d) provide additional evidence that the growth process is not thermally driven, but instead reflect the material's free energy landscape [20].

Accordingly, the absence of a second minimum in the energy landscape when no magnetic field is applied, and thus the absence of an energy barrier, suggests that no relaxation should be observed upon complete removal of the magnetic field. This coincides precisely with what is observed experimentally and shown in Fig. 4a) and b), and hence explains the asymmetric behavior of the lattice parameter and magnetization's relaxations.

3. Conclusion

In this work, we have extensively analyzed the kinetics of the structural component of the magnetovolume phase transition in a $LaFe_{11.6}Si_{1.4}$ sample, building upon prior knowledge derived from magnetic measurements. A strong influence of the applied magnetic field profile was observed in the time evolution of the magnetovolume coupled phase transition. The application of a sufficiently high magnetic field was capable of inducing the isostructural phase transition. However, when the magnetic field is paused at a field larger than the critical field H_{c1}, the lattice shows further relaxation in time (up to 300 s), significantly surpassing the relaxation times reported from magnetization measurements (up to 25 s under identical conditions) [20]. Increasingly higher lattice parameter relaxation rates and lower relaxation times are observed as the magnetic field is further increased above the critical field H_{c1}. The rate at which the magnetic field is applied was also observed to influence the relaxation time. Although faster applications resulted in longer relaxation times, the shorter field application period inherently associated to higher sweep rates compensates this increase, leading to an overall decrease in total transition time. While the sample's temperature played a key role in determining the lattice parameter at zero magnetic field, as well as the critical field at which the phase transition is initiated, we find the characteristics of the relaxation profiles of the lattice parameter to be largely independent of temperature, which contrasts with what has been reported for its magnetization counterpart.

Magnetic field cycling (allowing saturation of the lattice parameter following field application) revealed the lattice parameter to return to its initial value while the magnetic field had not yet been completely removed. This asymmetry of the phase transition dynamics during field application and removal was modeled by a suitable Hamiltonian which allowed the simulation of the Gibbs free energy landscape of the magnetization and lattice parameter for a wide range of temperatures and magnetic fields across the phase transition. During magnetic field application, the appearance of a second energetic local minimum gives rise to a metastable energy state which is shown to be responsible for the phase transition dynamics observed through correlation of the associated energy barriers and the observed relaxation times. Conversely, as the magnetic field is removed completely, the absence of a secondary minimum results in the lack of transition dynamics. Additionally, the temperature dependence of the relaxation time with respect to the energetic barrier is indicative of a growth process that is not thermally activated, but rather reflective of the intrinsic free energy landscape.

These findings prompt the necessity to further investigate the magnetic and structural dynamics of the phase transition in device engineering of magnetic refrigerators and thermomagnetic energy harvesters utilizing FOPT magnetocaloric materials, as these ought to reflect the phase transition asymmetry, characterized by significant structural relaxation times upon magnetic field application and their absence upon magnetic field removal. Furthermore, these also highlight the importance of a study comparing the magnetic and structural dynamics simultaneously, as well as analyzing in more detail the phase transition dynamics upon magnetic field removal up to its corresponding critical field.

4. Experimental section

The $LaFe_{11.6}Si_{1.4}$ sample was prepared by induction melting and subsequently subjected to a heat treatment at 1373 K for 1 week. Detailed magnetization measurements indicate that, at $\mu_0 H = 2$ T, the sample exhibits an adiabatic temperature change (ΔT_{ad}) of 5.9 K and an isothermal entropy change ($|\Delta S_{iso}|$) of 21.08 J kg^{-1} K^{-1}, in addition to a magnetic field dependence of the Curie Temperature ($dT_C/d\mu_0 H$) of 3.6 K T^{-1}, in good agreement with previous studies [28]. The sample was then hand milled, resulting in a median particle size of 4.5 μm with a standard deviation of 9.5 μm, as shown in Fig. S10 in the Supplemental Material.

The Curie Temperature of the alloy was measured to be 178.1 K upon cooling under a magnetic field of 0.01 T by acquiring X-ray diffraction patterns as a function of temperature at a temperature sweep rate of 1 K min^{-1}. The acquired patterns were analyzed by Rietveld refinements [62] employing a two-phase model with the software TOPAS [63,64].

The H_{pause} measurements were obtained by continuously acquiring X-ray diffraction patterns at the 28-ID-1 PDF beamline at the National Synchrotron Light Source II at Brookhaven National Laboratory with a wavelength of 0.1665 Å and a time resolution of 2 s during a complete magnetic field cycle (application, pause and removal) [55]. As such, diffraction patterns were continuously obtained during field application at 5.4 mT s^{-1} up to the value of H_{pause}, for the following 10 min, and then upon complete removal of the magnetic field at 5.4 mT s^{-1}, from H_{pause} down to 0 T, and for 5 min afterwards. Between measurements, a 5-min PM thermal reset at 218.1 K (T_C + 40 K) was performed and the sample was then cooled and allowed to reach a stable thermal equilibrium for 10 min at the desired measurement temperature, $T_C + T_0$. As shown in Fig. 1c), Rietveld refinements were performed to determine the structural evolution of the alloy as a function of time.

The magnetic measurements presented were performed using the VSM mode in a Quantum Design MPMS3 magnetometer following the protocol described above. Minor experimental deviations to the material's T_C brought about by the set-up were taken into account.

A similar protocol was also employed at the Wide-Angle Neutron Diffractometer (WAND^2) beamline at Oak Ridge National Laboratory [65,66] making use of the High Flux Isotope Reaction (HFIR) and utilizing a magnetic field sweep rate of 8.3 mT s^{-1}. The instrument was fitted with a Ge[113] monochromator providing a beam with an incident wavelength of 1.488676 Å. The detector bank was set to cover 2θ scattering angles from 4° to 124°, corresponding to a d-spacing in the range of 21.33 Å to 0.85 Å, and a momentum transfer (defined as 2π/d) from 7.4 Å $^{-1}$ to 0.3 Å $^{-1}$. The sample was loaded in a helium filled 6 mm diameter vanadium can and kept in place with a piece of neutron absorbing Gd paper, to minimize rotation due to magnetic field induced torque. The data collection at WAND^2 is made in event mode, allowing the inspection of time dependent behavior after data collection, and its processing was performed using the Mantid framework [67,68].

CRediT authorship contribution statement

André Azevedo Beleza: Writing – review & editing, Writing – original draft, Visualization, Software, Methodology, Investigation, Formal analysis. **Bernardo Pires:** Writing – review & editing, Visualization, Investigation, Formal analysis. **Rafael Almeida:** Writing – review & editing, Validation, Software, Methodology, Investigation, Data curation, Conceptualization. **John S.O. Evans:** Writing – review & editing, Software, Investigation, Formal analysis. **António M. dos Santos:** Writing – review & editing, Methodology, Data curation, Conceptualization. **Mathias Frontzek:** Resources, Project administration, Methodology. **Edmund Lovell:** Writing – review & editing, Supervision, Methodology, Investigation, Conceptualization. **Benedikt Beckmann:** Writing – review & editing, Validation, Methodology, Formal analysis, Data curation. **Konstantin Skokov:** Writing – review & editing, Supervision, Resources, Data curation, Conceptualization. **Oliver Gutfleisch:** Writing – review & editing, Supervision, Resources, Project administration, Funding acquisition, Data curation. **João Pedro Araujo:** Writing – review & editing, Supervision, Resources, Project administration, Funding acquisition. **A.M. Milinda Abeykoon:** Writing – review & editing, Validation, Supervision, Resources, Methodology, Investigation, Formal analysis, Data curation. **João S Amaral:** Writing – review & editing, Validation, Software, Resources, Project administration, Investigation, Funding acquisition, Formal analysis, Data curation. **João Horta Belo:** Writing – review & editing, Visualization, Validation, Supervision, Resources, Project administration, Methodology, Investigation, Funding acquisition, Formal analysis, Data curation, Conceptualization.

Declaration of competing interest

The authors declare the following financial interests/personal relationships which may be considered as potential competing interests: Joao H. Belo reports financial support was provided by Fulbright Portugal. If there are other authors, they declare that they have no known competing financial interests or personal relationships that could have appeared to influence the work reported in this paper.

Data availability

Data will be made available on request.

Acknowledgements

Work partially supported by the projects PTDC/EMETED/3099/2020, UIDP/04968/2020-Programático (https://doi.org/10.54499/UIDP/04968/2020), UIDB/04968/2020 (https://doi.org/10.54499/UIDB/04968/2020" id="intref0030b), LA/P/0095/2020 (https://doi.org/10.54499/LA/P/0095/2020), NECL-NORTE-010145-FEDER-022096, CERN/FISTEC/0003/2019 and the bilateral research fund grant SMARTX from Fundação para a Ciência e Tecnologia (FCT) and from and the Portuguese Association of Researchers and Student in the UK (PARSUK), Portugal, and within the scope of the project CICECO-Aveiro Institute of Materials, UIDB/50011/2020, UIDP/50011/2020 & LA/P/0006/2020, financed by national funds through the FCT/MCTES (PIDDAC). J.H. Belo also deeply acknowledges Fullbright Portugal for his Fulbright Visiting Scholar grant, and FCT for his contract DL57/2016, with reference SFRH-BPD-87430/2012, and DL57/2016/CP1454/CT0013, with reference 10.54499/DL57/2016/CP1454/CT0013, DOI: 10.54499/DL57/2016/CP1454/CT0013. R. Almeida acknowledges FCT for the PhD grant with reference 2022.13354.BD. A portion of this research used resources at the High Flux Isotope Reactor, a DOE Office of Science User Facility operated by the Oak Ridge National Laboratory. We acknowledge financial support by the Deutsche Forschungsgemeinschaft (DFG) within the CRC/TRR 270 (Project-ID 405553726).

Appendix A. Supplementary data

Supplementary data to this article can be found online at https://doi.org/10.1016/j.mtphys.2024.101388.

References

[1] A. Kitanovski, Energy applications of magnetocaloric materials, Adv. Energy Mater. 10 (2020): 1903741.
[2] A. Smith, C.R.H. Bahl, R. Bjørk, K. Engelbrecht, K.K. Nielsen, N. Pryds, Materials challenges for high performance magnetocaloric refrigeration devices, Adv. Energy Mater. 2 (2021) 1288.
[3] O. Gutfleisch, M.A. Willard, E. Brück, C.H. Chen, S.G. Sankar, J.P. Liu, Magnetic materials and devices for the 21st century: stronger, lighter, and more energy efficient, Adv. Mater. 23 (2011) 821.
[4] X. Moya, N.D. Mathur, Caloric materials for cooling and heating, Science 370 (2020) 797.
[5] T. Gottschall, K.P. Skokov, M. Fries, A. Taubel, I. Radulov, F. Scheibel, D. Benke, S. Riegg, O. Gutfleisch, Making a cool choice: the materials library of magnetic refrigeration, Adv. Energy Mater. 9 (2019): 1901322.
[6] C. Aprea, A. Greco, A. Maiorino, C. Masselli, The environmental impact of solid-state materials working in an active caloric refrigerator compared to a vapor compression cooler, Int. J. Heat Technol. 36 (2018) 1155.
[7] X. Moya, S. Kar-Narayan, N.D. Mathur, Caloric materials near ferroic phase transitions, Nat. Mater. 13 (2014) 439.
[8] L.D. Griffith, Y. Mudryk, J. Slaughter, V.K. Pecharsky, Material-based figure of merit for caloric materials, J. Appl. Phys. 123 (2018): 034902.
[9] R. Almeida, C. Amorim, J.S. Amaral, J.P. Araújo, J.H. Belo, Direct measurement of the magnetocaloric effect through time-dependent magnetometry, Phys. Rev. Appl. 18 (2022): 024081.
[10] V. Franco, J. Blázquez, J. Ipus, J. Law, L. Moreno-Ramírez, A. Conde, Magnetocaloric effect: from materials research to refrigeration devices, Prog. Mater. Sci. 93 (2018) 112.
[11] K.A. Gschneidner, V.K. Pecharsky, Magnetocaloric materials, Annu. Rev. Mater. Sci. 30 (2000) 387.
[12] F. Casanova, A. Labarta, X. Batlle, E. Vives, J. Marcos, L. Mañosa, A. Planes, Dynamics of the first-order magnetostructural transition in $Gd_5(Si_xGe_{1-x})_4$, Eur. Phys. J. B 40 (2004) 427.
[13] A. Barcza, M. Katter, V. Zellmann, S. Russek, S. Jacobs, C. Zimm, Stability and magnetocaloric properties of sintered $La(Fe, Mn, Si)_{13}Hz$ alloys, IEEE Trans. Magn. 47 (2011) 3391.
[14] T. Gottschall, D. Benke, M. Fries, A. Taubel, I.A. Radulov, K.P. Skokov, O. Gutfleisch, A matter of size and stress: understanding the first-order transition in materials for solid-state refrigeration, Adv. Funct. Mater. 27 (2017): 1606735.
[15] S. Pandey, A. Quetz, I.D. Rodionov, A. Aryal, M.I. Blinov, I.S. Titov, V. N. Prudnikov, A.B. Granovsky, I. Dubenko, S. Stadler, N. Ali, Magnetic, transport, and magnetocaloric properties of boron doped Ni-Mn-In alloys, J. Appl. Phys. 117 (2015): 183905.
[16] L.M. Moreno-Ramírez, C. Romero-Muñiz, J.Y. Law, V. Franco, A. Conde, I. A. Radulov, F. Maccari, K.P. Skokov, O. Gutfleisch, The role of Ni in modifying the order of the phase transition of $La(Fe,Ni,Si)_{13}$, Acta Mater. 160 (2018) 137.
[17] A.M. Pereira, E. Kampert, J.M. Moreira, U. Zeitler, J.H. Belo, C. Magen, P. A. Algarabel, L. Morellon, M.R. Ibarra, J.N. Gonçalves, J.S. Amaral, V.S. Amaral, J. B. Sousa, J.P. Araújo, Unveiling the (De)coupling of magnetostructural transition nature in magnetocaloric $R_5Si_2Ge_2$ (R=Tb, Gd) materials, Appl. Phys. Lett. 99 (2011): 132510.
[18] A.L. Pires, J.H. Belo, A.M.L. Lopes, I.T. Gomes, L. Morellón, C. Magen, P. A. Algarabel, M.R. Ibarra, A.M. Pereira, J.P. Araújo, Phase competitions behind the

giant magnetic entropy variation: $Gd_5Si_2Ge_2$ and $Tb_5Si_2Ge_2$ case studies, Entropy 16 (2014) 3813.
[19] F.W. Wang, G.J. Wang, F.X. Hu, A. Kurbakov, B.G. Shen, Z.H. Cheng, Strong interplay between structure and magnetism in the giant magnetocaloric intermetallic compound $LaFe_{11.4}Si_{1.6}$: a neutron diffraction study, J. Phys. Condens. Matter 15 (2003) 5269.
[20] E. Lovell, A.M. Pereira, A.D. Caplin, J. Lyubina, L.F. Cohen, Dynamics of the first-order metamagnetic transition in magnetocaloric $La(Fe,Si)_{13}$: reducing hysteresis, Adv. Energy Mater. 5 (2015): 1401639.
[21] J. Liu, J. Moore, K. Skokov, M. Krautz, K. Löwe, A. Barcza, M. Katter, O. Gutfleisch, Exploring $La(Fe,Si)_{13}$-based magnetic refrigerants towards application, Scripta Mater. 67 (2012) 584.
[22] J. Lyubina, R. Schäfer, N. Martin, L. Schultz, O. Gutfleisch, Novel design of $La(Fe,Si)_{13}$ alloys towards high magnetic refrigeration performance, Adv. Mater. 22 (2010) 3735.
[23] A. Waske, D. Dzekan, K. Sellschopp, D. Berger, A. Stork, K. Nielsch, S. Fähler, Energy harvesting near room temperature using a thermomagnetic generator with a pretzel-like magnetic flux topology, Nat. Energy 4 (2019) 68.
[24] D. Dzekan, A. Waske, K. Nielsch, S. Fähler, Efficient and affordable thermomagnetic materials for harvesting low grade waste heat, Apl. Mater. 9 (2021): 011105.
[25] E. Lovell, M. Bratko, A.D. Caplin, L.F. Cohen, Nucleation and dynamics of the metamagnetic transition in magnetocaloric $La(Fe,Mn,Si)_{13}$, J. Phys. D Appl. Phys. 50 (2017): 424004.
[26] N. Kramer, A. Provino, C. Hanley, C. Kubiak, A.K. Pathak, Magnetic properties of $LaFe_{2-x}Co_xSi$: a new two-phase naturally formed composite alloy, AIP Adv. 13 (2023): 025320.
[27] F.X. Hu, L. Chen, J. Wang, L.F. Bao, J.R. Sun, B.G. Shen, Particle size dependent hysteresis loss in La0.7Ce0.3Fe11.6Si1.4C0.2 first-order systems, Appl. Phys. Lett. 100 (2012): 072403.
[28] A. Fujita, S. Fujieda, Y. Hasegawa, K. Fukamichi, Itinerant-electron metamagnetic transition and large magnetocaloric effects in $La(Fe_xSi_{1-x})_{13}$ compounds and their hydrides, Phys. Rev. B 67 (2003): 104416.
[29] L.X. Bo, Z. Altounian, D.H. Ryan, Structure and magnetic transition of $LaFe_{13-x}Si_x$ compounds, J. Phys. Condens. Matter 15 (2003) 7385.
[30] F.X. Hu, B.G. Shen, J.R. Sun, Z.H. Cheng, G.H. Rao, X.X. Zhang, Influence of negative lattice expansion and metamagnetic transition on magnetic entropy change in the compound $LaFe_{11.4}Si_{1.6}$, Appl. Phys. Lett. 78 (2001) 3675.
[31] J. Liu, M. Krautz, K. Skokov, T.G. Woodcock, O. Gutfleisch, Systematic study of the microstructure, entropy change and adiabatic temperature change in optimized La-Fe-Si alloys, Acta Mater. 59 (2011) 3602.
[32] R.O. Fleming, S. Gonçalves, A. Davarpanah, I. Radulov, L. Pfeuffer, B. Beckmann, K. Skokov, Y. Ren, T. Li, J. Evans, J. Amaral, R. Almeida, A. Lopes, G. Oliveira, J. P. Araújo, A. Apolinário, J.H. Belo, Tailoring negative thermal expansion via tunable induced strain in La–Fe–Si-based multifunctional material, ACS Appl. Mater. Interfaces 14 (2022): 43498.
[33] D.Y. Karpenkov, A.Y. Karpenkov, K.P. Skokov, I.A. Radulov, M. Zheleznyi, T. Faske, O. Gutfleisch, Pressure dependence of magnetic properties in $La(Fe, Si)_{13}$: multistimulus responsiveness of caloric effects by modeling and experiment, Phys. Rev. Appl. 13 (2020): 034014.
[34] K.P. Skokov, A.Y. Karpenkov, D.Y. Karpenkov, I.A. Radulov, D. Günzing, B. Eggert, A. Rogalev, F. Wilhelm, J. Liu, Y. Shao, K. Ollefs, M.E. Gruner, H. Wende, O. Gutfleisch, A multi-stage, first-order phase transition in $LaFe_{11.8}Si_{1.2}$: interplay between the structural, magnetic, and electronic degrees of freedom, Appl. Phys. Rev. 10 (2023): 031408.
[35] B. Beckmann, D. Koch, L. Pfeuffer, T. Gottschall, A. Taubel, E. Adabifiroozjaei, O. N. Miroshkina, S. Riegg, T. Niehoff, N.A. Kani, M.E. Gruner, L. Molina-Luna, K. P. Skokov, O. Gutfleisch, Dissipation losses limiting first-order phase transition materials in cryogenic caloric cooling: a case study on all-d-metal Ni(-Co)-Mn-Ti Heusler alloys, Acta Mater. 246 (2023): 118695.
[36] A. Waske, L. Giebeler, B. Weise, A. Funk, M. Hinterstein, M. Herklotz, K. Skokov, S. Fähler, O. Gutfleisch, J. Eckert, Asymmetric first-order transition and interlocked particle state in magnetocaloric $La(Fe, Si)_{13}$, Phys. Status Solidi RRL 9 (2015) 136.
[37] L. Pfeuffer, T. Gottschall, T. Faske, A. Taubel, F. Scheibel, A.Y. Karpenkov, S. Ener, K.P. Skokov, O. Gutfleisch, Influence of the martensitic transformation kinetics on the magnetocaloric effect in Ni-Mn-In, Phys. Rev. Mater. 4 (2020): 111401.
[38] H. Neves Bez, K.K. Nielsen, A. Smith, P. Norby, K. Ståhl, C.R.H. Bahl, Strain development during the phase transition of $La(Fe,Mn,Si)_{13}H_z$, Appl. Phys. Lett. 109 (2016): 051902.
[39] Á. Díaz-García, L.M. Moreno-Ramírez, J.Y. Law, F. Albertini, S. Fabbrici, V. Franco, Characterization of thermal hysteresis in magnetocaloric NiMnIn heusler alloys by temperature first order reversal curves (TFORC), J. Alloys Compd. 867 (2021): 159184.
[40] A. Diestel, R. Niemann, B. Schleicher, S. Schwabe, L. Schultz, S. Fähler, Field-temperature phase diagrams of freestanding and substrate-constrained epitaxial Ni-Mn-Ga-Co films for magnetocaloric applications, J. Appl. Phys. 118 (2015): 023908.
[41] J. Döntgen, J. Rudolph, T. Gottschall, O. Gutfleisch, D. Hägele, Millisecond dynamics of the magnetocaloric effect in a first- and second-order phase transition material, Energy Technol. 6 (2018) 1470.
[42] R.M. Costa, E. Lovell, R. Almeida, R.M.C. Pinto, L.F. Cohen, A.M. Pereira, J. P. Araújo, J.H. Belo, Landau theory-based relaxational modeling of first-order magnetic transition dynamics in magnetocaloric materials, J. Phys. D Appl. Phys. 56 (2023): 155001.
[43] A. Davarpanah, J.H. Belo, V.S. Amaral, J.S. Amaral, On the optimization of magneto-volume coupling for practical applied field magnetic refrigeration, Phys. Status Solidi B 256 (2019): 1800419.
[44] M.D. Kuz'min, Factors limiting the operation frequency of magnetic refrigerators, Appl. Phys. Lett. 90 (2007): 251916.
[45] K. Qiao, J. Wang, S. Zuo, H. Zhou, J. Hao, Y. Liu, F. Hu, H. Zhang, A.G. Gamzatov, A. Aliev, C. Zhang, J. Li, Z. Yu, Y. Gao, F. Shen, R. Ye, Y. Long, X. Bai, J. Wang, J. Sun, R. Huang, T. Zhao, B. Shen, Enhanced performance of ΔTad upon frequent alternating magnetic fields in FeRh alloys by introducing second phases, ACS Appl. Mater. Interfaces 14 (2022): 18293.
[46] V. Franco, J. Blázquez, B. Ingale, A. Conde, The magnetocaloric effect and magnetic refrigeration near room temperature: materials and models, Annu. Rev. Mater. Res. 42 (2012) 305.
[47] J. Leib, J.E. Snyder, T.A. Lograsso, D. Schlagel, D.C. Jiles, Dynamics of the magnetic field-induced first order magnetic-structural phase transformation of $Gd_5(Si_{0.5}Ge_{0.5})_4$, J. Appl. Phys. 95 (2004) 6915.
[48] H.W. Zhang, F. Wang, T.Y. Zhao, S.Y. Zhang, J.R. Sun, B.G. Shen, Thermally activated itinerant metamagnetic transition in $LaFe_{11.7}Si_{1.3}$, Phys. Rev. B 70 (2004): 212402.
[49] V. Basso, M. Piazzi, C. Bennati, C. Curcio, Hysteresis and phase transition kinetics in magnetocaloric materials, Phys. Status Solidi B 255 (2018): 1700278.
[50] L.M. Moreno-Ramírez, J.S. Blázquez, I.A. Radulov, K.P. Skokov, O. Gutfleisch, V. Franco, A. Conde, Combined kinetic and Bean–Rodbell approach for describing fieldinduced transitions in $LaFe_{11.6}Si_{1.4}$ alloys, J. Phys. D Appl. Phys. 54 (2021): 135003.
[51] A. Fujita, K. Fukamichi, J.T. Wang, Y. Kawazoe, Large magnetovolume effects and band structure of itinerantelectron metamagnetic $La(Fe_xSi_{1-x})_{13}$ compounds, Phys. Rev. B 68 (2003): 104431.
[52] A. Terwey, M.E. Gruner, W. Keune, J. Landers, S. Salamon, B. Eggert, K. Ollefs, V. Brabänder, I. Radulov, K. Skokov, T. Faske, M.Y. Hu, J. Zhao, E.E. Alp, C. Giacobbe, O. Gutfleisch, H. Wende, Influence of hydrogenation on the vibrational density of states of magnetocaloric $LaFe_{11.4}Si_{1.6}$ $H_{1.6}$, Phys. Rev. B 101 (2020): 064415.
[53] M.E. Gruner, W. Keune, B. Roldan Cuenya, C. Weis, J. Landers, S.I. Makarov, D. Klar, M.Y. Hu, E.E. Alp, J. Zhao, M. Krautz, O. Gutfleisch, H. Wende, Element-resolved thermodynamics of magnetocaloric $LaFe_{13-x}Si_x$, Phys. Rev. Lett. 114 (2015): 057202.
[54] J. Landers, S. Salamon, W. Keune, M.E. Gruner, M. Krautz, J. Zhao, M.Y. Hu, T. S. Toellner, E.E. Alp, O. Gutfleisch, H. Wende, Determining the vibrational entropy change in the giant magnetocaloric material $LaFe_{11.6}Si_{1.4}$ by nuclear resonant inelastic x-ray scattering, Phys. Rev. B 98 (2018): 024417.
[55] D. Kramer, Brilliant new x-ray source is up and running at Brookhaven, Phys. Today 68 (2015) 20.
[56] See Supplemental Material at [URL will be inserted by publisher] for additional figures and detailed data that further support the presented findings.
[57] A. Fujita, Y. Akamatsu, K. Fukamichi, Itinerant electron metamagnetic transition in $La(Fe_xSi_{1-x})_{13}$ intermetallic compounds, J. Appl. Phys. 85 (1999) 4756.
[58] M. Avrami, Kinetics of phase change, J. Chem. Phys. 7 (1939) 1103.
[59] K. Shirzad, C. Viney, A critical review on applications of the Avrami equation beyond materials science, J. R. Soc., Interface 20 (2023): 20230242.
[60] Y. Mudryk, Y. Lee, T. Vogt, K.A. Gschneidner, V.K. Pecharsky, Polymorphism of $Gd_5Si_2Ge_2$: the equivalence of temperature, magnetic field, and chemical and hydrostatic pressures, Phys. Rev. B 71 (2005): 174104.
[61] J.S. Amaral, V.S. Amaral, Simulating the giant magnetocaloric effect-from mean-field theory to microscopic models, Front. Mater. 10 (2023).
[62] H.M. Rietveld, A profile refinement method for nuclear and magnetic structures, J. Appl. Crystallogr. 2 (1969) 65.
[63] A.A. Coelho, TOPAS and TOPAS-Academic: an optimization program integrating computer algebra and crystallographic objects written in C++, J. Appl. Crystallogr. 51 (2018) 210.
[64] R.E. Dinnebier, A. Leineweber, J.S.O. Evans, Rietveld Refinement: Practical Powder Diffraction Pattern Analysis Using TOPAS, De Gruyter, Berlin, Boston, 2019.
[65] M. Frontzek, K. Andrews, A. Jones, B. Chakoumakos, J. Fernandez-Baca, The wide angle neutron diffractometer squared (WAND2) – possibilities and future, Phys. B Condens. Matter 551 (2018) 464.
[66] M.D. Frontzek, R. Whitfield, K.M. Andrews, A.B. Jones, M. Bobrek, K. Vodopivec, B.C. Chakoumakos, J.A. Fernandez-Baca, WAND2—a versatile wide angle neutron powder/single crystal diffractometer, Rev. Sci. Instrum. 89 (2018): 092801.
[67] Mantid Project, Manipulation and Analysis Toolkit for Instrument Data, https://doi.org/10.5286/SOFTWARE/MANTID (accessed: August, 2023)..
[68] O. Arnold, J. Bilheux, J. Borreguero, A. Buts, S. Campbell, L. Chapon, M. Doucet, N. Draper, R. Ferraz Leal, M. Gigg, V. Lynch, A. Markvardsen, D. Mikkelson, R. Mikkelson, R. Miller, K. Palmen, P. Parker, G. Passos, T. Perring, P. Peterson, S. Ren, M. Reuter, A. Savici, J. Taylor, R. Taylor, R. Tolchenov, W. Zhou, J. Zikovsky, Mantid—data analysis and visualization package for neutron scattering and μ SR experiments, Nucl. Instrum. Methods Phys. Res., Sect. A 764 (2014) 156.